International Journal for Housing Science and Its Applications
Publish September 8, 2025. Volume 47, Issue 1 Pages 60-69

https://doi.org/10.70517/ijhsa47105

Research on the Application of Spatio-Temporal Analysis Methods Based on Artificial Intelligence Remote Sensing Data in Urban Monitoring

Yan Zhang[1,2], Yunkun Zou[1,2,*], Lingyuan Zhao[1,2], Yuhan Jiang[1,2], Shisen Liao[1,2] and Zifei Luo[1,2]

[1] HuanTian Wisdom Technology Co., Ltd., Meishan, Sichuan, 620564, China
[2] Joint Laboratory of Spatial Intelligent Perception and Large Model Application, Nanjing University of Aeronautics and Astronautics & HuanTian Wisdom Technology Co., Ltd., Meishan, Sichuan, 620564, China

Corresponding authors: (e-mail: zouyk@htwisdom.cn).

Abstract Taking Xiamen, a densely populated city with rapid economic development, as an example, this study employs surface temperature data derived from MODIS remote sensing data optimized through remote sensing and artificial intelligence technologies to extract urban heat island and vegetation coverage information. The study conducts dynamic monitoring and spatiotemporal analysis of the urban heat island in the study area. Taking Yunnan Province as another example, based on Landsat OLI/TM and NPP_VIIRS remote sensing data, the study extracts urban built-up area information and examines the expansion characteristics of urban built-up areas from three aspects: the number of expansions, spatial distribution patterns, and nighttime light scale, covering the period from 2000 to 2020. Remote sensing data based on urban heat islands indicate that high-temperature zones are primarily distributed in densely populated urban areas with developed industries and commerce, while secondary high-temperature zones are scattered in the urban-rural fringe areas surrounding high-temperature zones. Areas with better water bodies and vegetation exhibit low-temperature and secondary low-temperature conditions. For example, parts of Xiamen's urban core are primarily controlled by high-temperature and secondary high-temperature zones. Remote sensing data based on urban expansion indicate that there are significant differences in expansion rates and intensities across different cities and stages. For instance, the expansion intensity of the Dianzhong Urban Agglomeration generally follows a trend of “first decreasing—then increasing—and finally decreasing again.”

Index Terms remote sensing data, artificial intelligence, urban monitoring, urban heat island, urban expansion

I. Introduction

This paper first takes the rapidly urbanizing Xiamen region in 2019 and 2022 as an example to preprocess MODIS satellite remote sensing data for the region. Based on the inversion of land surface temperature (LST) from meteorological satellite data, the split-window algorithm suitable for MODIS data is adopted to invert LST according to the characteristics of the data and the actual conditions of the study area. To reveal the spatial distribution and interannual changes of the urban heat island in the study area, dynamic changes in vegetation were extracted, and a correlation analysis model between surface temperature and vegetation parameters was established. Subsequently, the annual growth rate and expansion dynamics index were used to reflect changes in the quantity of urban built-up areas. The spatial center of gravity shift model and expansion direction were then employed to investigate changes in the spatial distribution patterns of urban built-up areas. Finally, the economic development within urban built-up areas was reflected from the perspective of nighttime light scale changes.

II. Spatio-temporal analysis methods for remote sensing data based on urban monitoring

II. A. Data preprocessing

This study utilizes MODIS satellite remote sensing data from 2019 and 2022 for Xiamen region under clear or mostly clear sky conditions [1]. Xiamen is located in the subtropical monsoon climate zone, where cloudy and rainy weather is prevalent throughout the year, making it challenging to obtain high-quality MODIS imagery. A survey revealed that there are approximately 5 to 20 MODIS images with relatively clear skies in the Xiamen region. Each year's MODIS imagery was processed through a synthesis method. First, cloud detection was performed on each MODIS image, and appropriate markings were applied. Then, the channel detection data from non-cloud pixels in each year's imagery were arithmetically averaged to create a synthetic MODIS image with the maximum possible clear-sky coverage. The maximum value synthesis method was employed to minimize atmospheric attenuation effects and obtain satellite data with reduced random noise interference. Before applying the synthesized images, the data must undergo preprocessing. MODIS data preprocessing includes Bowtie Effect processing, stripe removal, data calibration, projection conversion, and geometric correction.

II. B. Dynamic monitoring of urban remote sensing data based on urban heat islands

II. B. 1) Inversion of surface temperature

Based on the inversion of land surface temperature (LST) from meteorological satellite data [2], the split-window algorithm suitable for MODIS data was used to invert the land surface temperature according to the characteristics of the data and the actual conditions of the study area. The formula is as follows:

$$LST = C_0 + C_1 \cdot T_{31} - C_2 \cdot T_{32} \tag{1}$$

$$C_0 = -64.60363 Z_1 + 68.7255 Z_2 \tag{2}$$

$$C_1 = 1 + Z_0 + 0.44081 Z_1 \tag{3}$$

$$C_2 = Z_0 + 0.473453 Z_1 \tag{4}$$

$$Z_0 = \frac{Y_{31}}{X_{31} \cdot Y_{32} - X_{32} \cdot Y_{31}} \tag{5}$$

$$Z_1 = \frac{Y_{32}(1 - X_{31} - Y_{31})}{X_{31} \cdot Y_{32} - X_{32} \cdot Y_{31}} \tag{6}$$

$$Z_2 = \frac{Y_{31}(1 - X_{32} - Y_{32})}{X_{31} \cdot Y_{32} - X_{32} \cdot Y_{31}} \tag{7}$$

In the equation, LST, T_{31}, and T_{32} represent surface temperature, brightness temperature of MODIS channels 31 and 32, respectively, while $C_0, C_1, C_2, Z_0, Z_1, Z_2$ are the split-window algorithm parameters, and $X_{31}, X_{32}, Y_{31}, Y_{32}$ can be calculated using the following equation:

$$X_i = \varepsilon_i \cdot \tau_i \tag{8}$$

$$Y_i = (1 - \tau_i)[1 + (1 - \varepsilon_i)\tau_i] \tag{9}$$

Among these, i represents MODIS bands 31 and 32, ε_i denotes the surface emissivity, and τ_i denotes the atmospheric transmittance.

For MODIS pixels with a resolution of 255 m, it can be assumed that they are composed of a mixture of water bodies, vegetation, and bare soil with different area proportions. The surface emissivity ε can be estimated using the following equation:

$$\varepsilon i = P_w \cdot K_w \cdot \varepsilon_{wi} + P_v \cdot K_v \cdot \varepsilon_n + (1 - P_w - P_v) \cdot K_s \cdot \varepsilon_{si} \tag{10}$$

In the equation, $\varepsilon_{wi}, \varepsilon_{vi}$ and ε_{si} are the emissivity ratios of water bodies, vegetation, and bare soil, respectively, while K_w, K_v and K_s are the temperature ratios of water bodies, vegetation, and bare soil, respectively. P_w and P_v are the area proportions of water bodies and vegetation in the mixed pixel, respectively. For pure water body pixels, $P_w = 1$, and for non-pure water body pixels, $P_w = 0$. P_v is obtained by converting the vegetation coverage.

Atmospheric transmittance τ is estimated using empirical formulas. Since atmospheric transmittance is primarily influenced by atmospheric water vapor content, the following empirical formulas are used to estimate the atmospheric transmittance of MODIS channels 31 and 32, respectively:

$$\tau_{31} = -0.10671 \left[(0.02 - \ln \frac{R_{19}}{R_2}) / 0.65 \right]^2 + 1.04015 \tag{11}$$

$$\tau_{32} = -0.12577 \left[(0.02 - \ln \frac{R_{19}}{R_2}) / 0.65 \right]^2 + 0.99229 \tag{12}$$

II. B. 2) Extraction of heat island areas and vegetation indices

To reveal the spatial distribution and interannual changes of the urban heat island in the study area, this paper further processes the inverted surface temperature images. Since vegetation can reduce heat in the soil or on the ground surface through transpiration, playing an important role in lowering surface temperatures, this study extracts dynamic vegetation change information from the study area, establishes a correlation analysis model between surface temperature and vegetation parameters, and explores the interactive relationship between the urban heat island and vegetation cover. Vegetation indices can quantitatively reflect the biomass and coverage of ground vegetation, serving as indicators of plant growth status and vegetation spatial distribution density. The most widely used index is the Normalized Difference Vegetation Index (NDVI):

$$NDVI = \frac{R_{nir-R_{red}}}{R_{nir+R_{red}}} \tag{13}$$

Among them, R_{nir} and R_{red} are the reflectance of the near-infrared band and the red light band, respectively.

II. C. Dynamic monitoring of urban remote sensing data based on urban expansion

This section uses remote sensing data from Yunnan Province for the years 2000, 2005, 2010, 2015, and 2020 as the research subject. It selects five non-radiometric calibrated nighttime light images from the F12000, F22005, F32010, F42015, and F52020, which were taken at five-year intervals between 1999 and 2020, to monitor and analyze the spatiotemporal patterns of urban areas.

II. C. 1) Analysis of urban built-up areas

(1) Extraction of urban built-up areas

The normalized building index [3] (NDBI) utilizes Landsat OLI/TM images to automatically extract information on built-up areas based on the characteristics that most land types have lower gray values in the infrared and near-infrared bands, while gray values for built-up areas increase. The formula is as follows:

$$NDBI = \frac{band5 - band4}{band5 + band4} \tag{14}$$

In the formula, band4 and band5 are the 4th and 5th bands of the TM image, respectively.

Using the method proposed by Tang, Liangbo, et al., the normalized difference vegetation index (NDVI) and NPP-VIIRS nighttime images were introduced to remove interfering objects and improve the accuracy of built-up area extraction.

The formula for the urban land use index (UCLI) is as follows:

$$UCLI = NL \times NDVI \times NDBI \tag{15}$$

A UCLI value of 0 indicates non-built-up land, while a value of 1 indicates built-up land. Using UCLI, the boundaries of built-up areas at different time periods are extracted, and then continuous built-up area boundaries are delineated based on the obtained boundaries.

(2) Number of urban built-up area expansions

Expansion rate analysis: The annual growth rate is selected to reflect the quantitative evolution of the built-up area through changes in its area at each stage, thereby understanding the overall trend of its expansion and evolution. The formula is as follows:

$$L = \frac{S_b - S_a}{T} \tag{16}$$

where: L is the annual average expansion rate of the city, S_a, S_b are the built-up areas of the city at the beginning and end of the study period, and T is the study period.

Expansion dynamic analysis: Expansion dynamics is calculated as the relative dynamic change rate of the expansion of the built-up area of a city, reflecting the relative speed of urban expansion. The formula is as follows:

$$R = \frac{S_b - S_a}{S_a \times T} \times 100\% \tag{17}$$

where: R represents the dynamic degree of built-up area expansion. Based on the research of numerous scholars, built-up area expansion is classified into five types according to the level of the expansion dynamics index: high-speed expansion

(>30%), rapid expansion (30% ≥ K > 20%), medium-speed expansion (20% ≥ K > 10%), low-speed expansion (10% ≥ K > 5%), and slow expansion (5% ≥ K).

(3) Analysis of changes in the spatial distribution pattern of urban built-up areas

Spatial center of gravity shift analysis: The spatial center of gravity shift model is an important method for analyzing the evolution of urban spatial distribution during the expansion of urban built-up areas. The formula for calculating the spatial center of gravity position of urban built-up areas at different time periods is as follows:

$$\bar{x}_i = \frac{\sum_{i=1}^{n}(A_{ii} \times X_i)}{\sum_{i=1}^{n} A_{ni}} \quad \bar{y}_i = \frac{\sum_{i=1}^{n}(A_{ni} \times Y_i)}{\sum_{i=1}^{n} A_n} \tag{18}$$

The formula for calculating the distance of the spatial center of gravity shift in urban built-up areas is as follows:

$$D = \sqrt{(\overline{x_{t+1}} - \bar{x}_t)^2 + (\overline{y_{t+1}} - \bar{y}_t)^2} \tag{19}$$

Among these: $(\bar{x}_i, \bar{y}_i), (\overline{x_{i+1}}, \overline{y_{i+1}})$ represent the spatial center coordinates of the urban built-up area in periods t and $t+1$, respectively; X_i denotes the horizontal coordinate of the i th geographical unit of the urban built-up area, and Y_i denotes the vertical coordinate of the i th geographical unit of the urban built-up area; A_n denotes the area of the i th geographical unit of the urban built-up area at time t; D denotes the distance of the spatial center of gravity of the urban built-up area from period t to $+1$.

Expansion direction analysis: Using the quadrant analysis method, the urban built-up area vectors are overlaid, and the urban built-up area is divided into eight directions based on four quadrants: north (N), northeast (NE), east (E), southeast (SE), south (S), southwest (SW), west (W), and northwest (NW). The changes in the built-up area for each direction are then calculated.

II. C. 2) Analysis of changes in the economic scale within urban built-up areas

Nighttime remote sensing imagery primarily includes two attributes: the size of the nighttime light distribution area and the intensity of nighttime light. If the nighttime light area is larger and the pixel brightness value is higher, it indicates a higher overall level of economic development in the region. The experiment utilized nighttime light analysis to evaluate the level of economic development within urban built-up areas, selecting evaluation indicators including nighttime light intensity and nighttime light average.

Nighttime light intensity (T) refers to the sum of all pixel $(x_i)DN$ values within the urban built-up area, which directly reflects the strength of human socio-economic activities within the built-up area. The calculation formula is as follows:

$$T = \sum_{i=1}^{n} x_i \tag{20}$$

where: x_i is the DN value of the i th pixel, and n is the total number of pixels in the area.

The nighttime luminance average (M) is the average DN value of all pixels (x_i) within the urban built-up area, reflecting the average level of socioeconomic activity intensity. This avoids the limitations of evaluating urban development levels solely based on the size of the built-up area. Its calculation method is as follows:

$$M = \frac{T}{n} \tag{21}$$

III. Application of spatio-temporal analysis methods for remote sensing data in urban monitoring

III. A. Comparison of surface temperature inversion results from different algorithms

The surface temperatures of the study area obtained using different algorithms are shown in Table 1, including the radiative transfer equation method (LSTRTE), image-based inversion algorithm (LST-IB), single-window algorithm (LST-MW), and universal single-channel algorithm (LST-SC). It can be concluded that, overall, the results obtained from the four algorithms show a similar trend. However, the IB algorithm yields lower temperatures, while the MW and RTE algorithms produce moderate results, and the SC algorithm yields the highest temperatures. The surface temperatures derived from all four algorithms are higher than the brightness temperatures detected by sensors at satellite altitude. After comprehensive comparison, this paper concludes that the results obtained using the MW algorithm for surface temperature inversion in the study area are more reasonable than those from the other algorithms. Therefore, the MW algorithm is adopted for temperature inversion calculations in the study area.

Table 1: The surface temperature of the research area of different algorithms

Bright temperature and inversion algorithm	Minimum value	Maximum value	Mean	Standard deviation
BT	16.093	35.213	23.803	2.7451
LST-IB	17.811	38.019	25.049	3.1665
LST-RTB	19.509	39.543	27.141	2.8818
LST-MW	18.331	28.495	25.967	3.123
LST-SC	20.956	40.948	29.12	2.7342

III. B. Spatio-temporal analysis of urban heat islands in the study area

III. B. 1) Definition of urban heat islands

According to the mean-standard deviation theory, the inverted surface temperature images are divided into 4, 5, and 6 levels using the combination of μ (mean), std (standard deviation), and Ts (true surface temperature). The method of dividing surface temperature levels using the mean-standard deviation method is shown in Table 2. Using the mean-standard deviation method, the annual surface temperature of the study area was divided into 4, 5, and 6 levels, and the classification results were compared and analyzed. In terms of the spatial distribution of urban heat islands, the study area was divided into 4 temperature levels. The high-temperature zone and the second-highest temperature zone were defined as heat island areas. However, the heat island areas were too large, the medium-temperature zone was extremely small, and the second-highest temperature zone was too average, which did not align with reality; When the study area is divided into 5 temperature levels, the high-temperature zone and sub-high-temperature zone are similarly defined as the heat island range. Compared to the level-based classification, the heat island range is reduced, the distribution of medium- and low-temperature zones is more reasonable, and the details of surface temperature variation are more prominently displayed; The study area is divided into five temperature levels, with the heat island zone corresponding to the extremely high-temperature zone and the high-temperature zone. The extremely high-temperature zone is too large, clearly inconsistent with reality. Although the temperature differences between different landforms are more pronounced compared to the level classification, the ground temperature information is too fragmented to facilitate the summary of patterns.

Table 2: The mean standard deviation method divides the temperature level

Fractional number	Temperature grade					
	Special region	High temperature region	Hypothermal zone	Medium temperature area	Secondary temperature zone	Cryogenic region
4 stage	—	$Ts>\mu+std$	$\mu<Ts\leq\mu+std$	$\mu-std<Ts\leq\mu$	—	$Ts<\mu-std$
5 stage	—	$Ts>\mu+std$	$\mu+0.55std<Ts\leq\mu+std$	$\mu-0.55std<Ts\leq\mu+std$	$\mu-std<Ts\leq\mu-std$	$Ts<\mu-std$
6 stage	$Ts>\mu+std$	$\mu+0.5std<Ts\leq\mu+std$	$\mu<Ts\leq\mu+0.55std$	$\mu-0.55std<Ts\leq\mu$	$Ts\leq-0.55std$	$Ts<\mu-std$

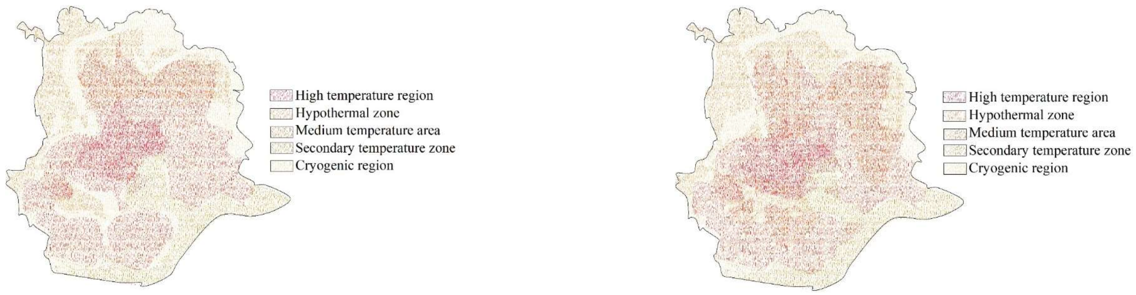

(a)October 10, 2019 (b)November 6, 2022

Figure 1: The surface temperature level of the study area

III. B. 2) Spatio-temporal pattern analysis of urban heat islands

(1) Spatial Characteristics Analysis of Urban Heat Islands

Based on the aforementioned surface temperature inversion and urban heat island definition experiments, the study divided the urban surface temperature data obtained from the inversion into five levels according to their mean values. High-temperature zones and sub-high-temperature zones were then defined as heat island zones, and a spatial pattern analysis of urban heat islands was conducted.

The surface temperature levels for October 10, 2019, and November 6, 2022, in the study area are shown in Figure 1, where (a) and (b) represent October 10, 2019, and November 6, 2022, respectively. It can be observed that high-temperature zones are primarily distributed in densely populated urban areas with developed industry and commerce. Sub-high-temperature zones are scattered in the urban-rural fringe areas surrounding high-temperature zones, while areas with better water bodies and vegetation exhibit low-temperature and sub-low-temperature conditions.

Using the results of heat island zone extraction and vegetation cover index as examples, this study analyzes the spatiotemporal patterns of urban heat islands in the Xiamen region. The distribution results of heat island zones on October 10, 2019, and November 6, 2022, in the study area are shown in Figure 2, where (a) and (b) represent October 10, 2019, and November 6, 2022, respectively. The results indicate that in 2019 and 2022, the urban heat islands in Xiamen primarily corresponded to the built-up areas, while the main urban core areas were primarily influenced by high-temperature zones and secondary high-temperature zones. Heat island zones are primarily distributed in the northwest of Xiamen Island, including Huliu District, Datong Town in Tong'an District, Xinglin Town and Jimei Subdistrict in Jimei District, Haicang Town in Haicang District, and Xindian Town in Xiang'an District. This is closely related to the geographical environment, vegetation coverage density, and water source distribution of different cities. The higher the vegetation coverage and the closer the city is to water sources, the less pronounced the urban heat island effect becomes.

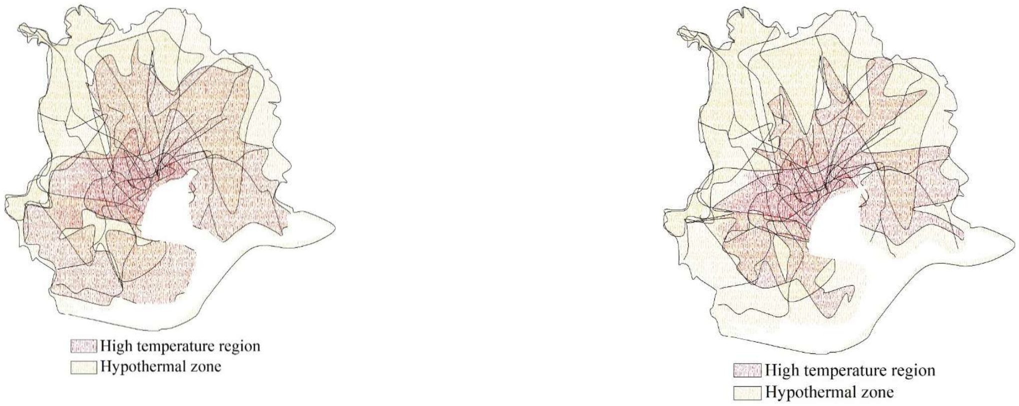

(a)October 10, 2019

(b)November 6, 2022

Figure 2: The results of the study of the heat island of the study

The results of changes in heat island areas across various districts of Xiamen City from 2019 to 2022 are shown in Table 3. It can be seen that Tong'an District has the largest heat island area, reaching 236.62 km^2 in 2019 and 235.11 km^2 in 2022; although Huliu District has a smaller heat island area, it has the highest heat island ratio, reaching 77.35% in 2019 and 82.46% in 2022. The changes in heat island area from 2019 to 2022 show that the heat island areas in Huliu District and Xiang'an District have increased annually, while those in the other four districts have decreased.

Table 3: The results of the area of the hot island of xiamen in 2022

Region	The hot island area of 2019		The hot island area of 2022		2019-2022 thermal island changes	
	Area (km^2)	Proportion (%)	Area (Km^2)	Proportion (%)	Area (Km^2)	Proportion (%)
Siming area	43.55	60.12	37.81	51.52	-5.74	-8.6
Haicang area	76.79	47.55	67.32	39.69	-9.47	-7.86
Huli area	45.61	77.35	49.02	82.46	3.41	5.11
Jimei area	107.58	42.85	104.57	42.48	-3.01	-0.37
Tongan area	236.62	37.13	235.11	37.22	-1.51	0.09
Xiang an area	147.13	42.91	160.54	50.73	13.41	7.82

(2) Analysis of the temporal characteristics of urban heat islands

This paper uses the urban heat island ratio index method for normalization, converting the inverted temperature range to a range between 0 and 1, i.e.:

$$N_i = \frac{T_{si} - T_{s\min}}{T_{s\max} - T_{s\min}} \tag{22}$$

In the equation, N_i is the normalized value of the i th pixel, Ts_i represents the surface temperature value of the i th pixel, and $Ts_{\max}$ and $Ts_{\min}$ are the maximum and minimum surface temperature values, respectively.

The difference between the normalized surface temperature images of the two scenes is calculated to generate a difference image map. The difference results of the heat island changes in the study area on October 10, 2019, and November 6, 2022, are shown in Figure 3. The figure clearly shows the changes in surface temperature in the study area from 2019 to 2022. Overall, over the four years, the areas with temperature increases were significantly larger than those with temperature decreases. From an internal perspective, the areas with temperature increases were concentrated in the main urban areas of each district, while the areas with temperature decreases were concentrated in water bodies, inland areas with good vegetation coverage, and the Ma Xiang and Xin Dian towns in Xiang'an District.

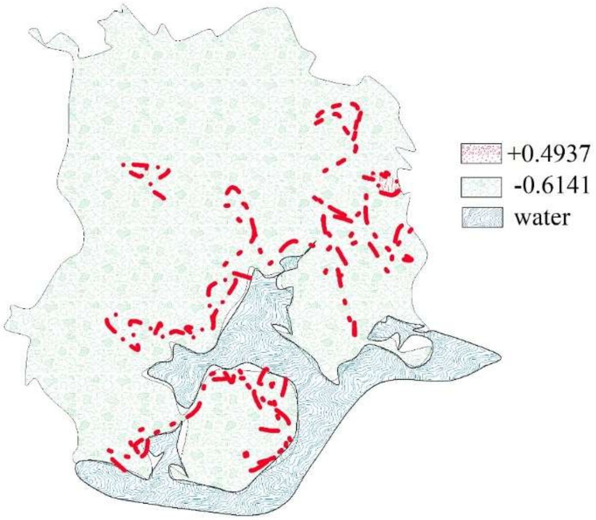

Figure 3: The difference of the difference in the heat island of the study area

III. C. Dynamic Monitoring of Urban Built-up Areas and Spatio-temporal Pattern Evolution

III. C. 1) Evaluation of the accuracy of built-up area extraction

The results of the quantitative accuracy evaluation are shown in Table 4. A1 represents the built-up area based on statistical data, A2 represents the built-up area based on Google Earth imagery, and A3 represents the built-up area extracted from nighttime light imagery. The absolute error between the statistical data built-up area A1 and the Google Earth imagery area A2 is C1, and the relative error is R1; the absolute error between the statistical data built-up area A1 and the urban built-up area A3 extracted from nighttime light imagery is C2, and the relative error is R2; the absolute error between the Google Earth imagery area A2 and the urban built-up area A3 extracted from nighttime light imagery is C3, and the relative error is R3. By comparing the built-up area in the statistical data of each city, the area extracted from Google Earth imagery data, and the land use area extracted from DMSP/OLS nighttime light remote sensing imagery for each city, the results show: the maximum absolute error between A1 and A2 is 19.04 km^2, and the maximum relative error is 8.69%; the maximum absolute error between A1 and A3 is -11.75 km^2, and the maximum relative error is -4.51%; A2A3 had the largest absolute error of -15.43 km^2 and the largest relative error of -8.63%. The relative errors between the built-up areas of the three methods were all less than 10%, indicating that the optimal threshold determined based on statistical data for extracting built-up area has relatively high accuracy.

III. C. 2) Analysis of the spatial pattern of urban agglomerations

(1) Spatial Changes in Urban Areas of the Dianzhong Urban Agglomeration

According to statistics, the number of urban pixels in the Dianzhong region has been steadily increasing from 2000 to 2020. In 2000, the number of urban pixels in the Dianzhong region was 335, and by 2010, it had increased to 1,086. and 2,435 in 2020. Over the 20-year period, the number of built-up area pixels in the Dianzhong region increased by 2,015, with the urban area expanding by nearly sixfold. The original urban area in the Dianzhong region has been growing steadily, while new small and medium-sized cities and emerging towns continue to emerge, leading to an increase in the number of built-up area pixels and the ongoing expansion of urban boundaries.

Table 4: Quantitative accuracy evaluation results

Year	2000	2005	2010	2015	2020
A1(km^2)	98.09	130.95	184.98	349.17	503.04
A2(km^2)	100.16	143.13	192.78	331.93	522.08
A3(km^2)	97.54	130.54	177.35	337.42	510.25
C1(km^2)	2.07	12.18	7.81	-17.24	19.04
C2(km^2)	-0.55	-0.41	-7.63	-11.75	7.21
C3(km^2)	-2.62	-12.59	-15.43	5.49	-11.83
R1(%)	2.78	8.69	4.56	-4.68	3.78
R2(%)	-0.22	0.98	-4.51	-3.35	1.38
R3(%)	-2.48	-7.06	-8.63	1.64	-2.23

(2) Spatial pattern of the Dianzhong urban agglomeration

To further explore the urban pattern formed in the Dianzhong region over the past 20 years, this paper overlays the 2020 built-up areas of the Dianzhong urban agglomeration with the main highways in the Dianzhong region. It was found that the distribution of built-up area patches in the Dianzhong region forms a pattern where highways serve as skeletal corridors, with patches scattered around the highways. The spatial structure of the Dianzhong Urban Agglomeration in 2020 is shown in Figure 4. The distribution pattern of the built-up areas in the entire Dianzhong region is centered on Kunming City, roughly forming three urban development axes: "Kunming-Qujing," "Kunming-Chuxiong," and "Kunming-Yuxi-Mengzi." The urban agglomeration exhibits a "central radiating" pattern.

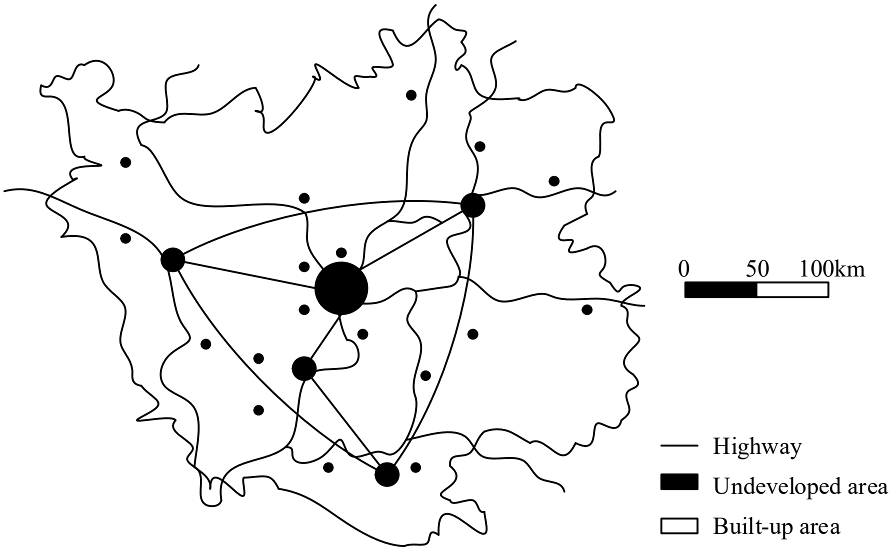

Figure 4: Spatial Structure of the urban agglomeration in central Yunnan in 2020

III. C. 3) Analysis of Urban Expansion in Central Yunnan

(1) Changes in Form and Direction

Through spatial overlay analysis of the results of built-up area extraction for Kunming, Qujing, Chuxiong, and Yuxi in the Yunnan Central Urban Agglomeration for the years 2000, 2005, 2010, 2015, and 2020, the expansion patterns of major cities in the Yunnan Central region from 2000 to 2020 are shown in Figure 5. It was found that Kunming City has been expanding outward from its central urban area, with the primary expansion directions being the Chenggong New District to the southeast and the Airport District to the northeast of the city; Qujing City's primary expansion direction is toward the northern Zhan Yi District; Chuxiong City exhibits a southeast-to-northwest stretching expansion pattern; and Yuxi City expands in a fan-shaped pattern centered on the Hongta District, with the primary expansion directions being southwest to northeast.

(2) Changes in area

Using DMSP/OLS nighttime light data to extract statistics on changes in built-up area, it was found that over the past 20 years, the city with the largest increase in urban area in the central Yunnan region was Kunming, followed by Qujing, Yuxi, and Chuxiong. Between 2000 and 2020, the built-up area of Kunming increased by 412.71 km^2, that of Qujing by 160.6 km^2, that of Yuxi by 75.05 km^2, and that of Chuxiong by 71.98 km^2. Except for these four major cities, the area changes of other smaller towns in the Dianzhong region remained relatively stable during this period.

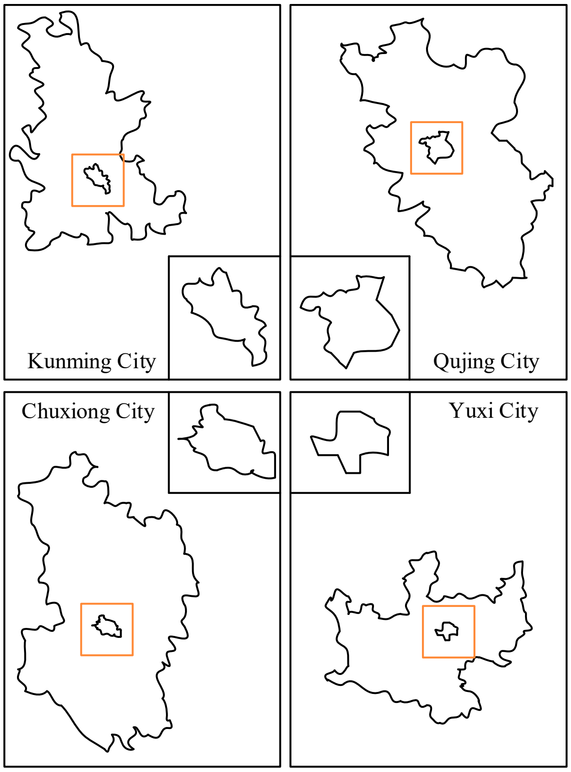

Figure 5: Expansion patterns of Major cities in central Yunnan from 2000 to 2020

(3) Changes in Rate and Intensity

The intensity of urban expansion in the Dianzhong region is shown in Table 5. It can be observed that prior to 2010, cities in the Dianzhong region were in a slow growth phase, entered a rapid growth phase after 2010, and experienced a slower growth rate but maintained a stable rapid growth trend after 2015. Among them, Kunming City had the fastest expansion rate at 34.43 km²/year, while Qujing City had the fastest expansion rate at 20.57 km²/year. Chuxiong City and Yuxi City had relatively slower expansion rates, with Chuxiong City reaching a maximum expansion rate of 6.97 km²/year and Yuxi City reaching a maximum expansion rate of 6.85 km²/year.

By calculating the urban expansion intensity index for the Dianzhong urban agglomeration, it was found that the overall trend in urban expansion intensity over the 20-year period was "first decreasing, then increasing, and then decreasing again." Among these, the spatial expansion intensity of Qujing City's built-up area showed significant changes, decreasing slightly before 2010 and then beginning to rise, reaching a peak in 2015 before entering a decreasing phase. The urban expansion intensity of Kunming City, Chuxiong City, and Yuxi City remained relatively stable, with peaks occurring between 2010 and 2020.

Table 5: Urban expansion intensity

City	Year	A/km^2	a/km^2	At/%	Vt/(km^2·a^{-1})	Ca
Kunming city	2000	97.54	—	—	—	—
	2005	130.54	33	35.57	6.98	7.1
	2010	177.35	46.81	33.08	8.82	6.6
	2015	337.42	160.07	90.96	31.82	18.17
	2020	510.25	172.83	51.24	34.43	10.28
Qujing city	2000	16.57	—	—	—	—
	2005	23.89	7.32	43.98	1.33	8.73
	2010	25.75	1.86	8.39	0.5	1.52
	2015	127.08	101.33	392.06	20.57	78.6
	2020	177.17	50.09	38.91	10.07	7.84
Chuxiong city	2000	16.08	—	—	—	—

	2005	15.95	0.00	0.00	0.00	0.00
	2010	24.93	8.98	55.99	1.69	11.21
	2015	60.78	35.85	144.01	6.97	28.98
	2020	88.06	27.28	44.82	5.47	9.00
Yuxi city	2000	5.78	—	—	—	—
	2005	16.24	10.46	166.66	1.93	33.37
	2010	20.02	3.78	24.86	0.78	5.09
	2015	53.35	33.33	167.84	6.85	33.61
	2020	80.83	27.48	51.04	5.47	10.23

IV. Conclusion

This paper takes Xiamen and Yunnan Province as examples and uses remote sensing data obtained through artificial intelligence technology to conduct dynamic monitoring and spatiotemporal analysis of urban heat island effects and expansion rates. The results show:

(1) The distribution of high-temperature areas in cities is closely related to population density, industrial and commercial development, water bodies, and vegetation coverage. For example, in 2019 and 2022, the urban heat island in Xiamen City largely corresponded to the built-up areas, while the main urban areas were primarily influenced by high-temperature and secondary high-temperature zones. Heat island zones were mainly distributed in the northwest of Xiamen Island, including Huliu District, Datong Town in Tong'an District, Xinglin Town and Jimei Subdistrict in Jimei District, Haicang Town in Haicang District, and Xindian Town in Xiang'an District.

(2) The rise and fall of urban surface temperatures are directly related to water bodies and inland vegetation coverage. Over the past 20 years, the areas in Xiamen where urban temperatures have risen are significantly larger than those where temperatures have decreased. The areas with rising temperatures are concentrated in the main urban areas of each district, while the areas with decreasing temperatures are concentrated in regions with better water body and inland vegetation coverage.

(3) The intensity and speed of urban expansion are related to time and the area of the built-up zone. Over the past 20 years, the overall trend of expansion intensity in the Dianzhong Urban Agglomeration has been “first decreasing—then increasing—and then decreasing again.” Among these, the spatial expansion intensity of the built-up zone in Qujing City has shown significant changes, with a slight decrease before 2010, followed by an increase, reaching a peak in 2015, and then entering a decreasing phase.

Funding

This research was Supported by Open Project Funds for the Joint Laboratory of Spatial Intelligent Perception and Large Model Application (Grant No. SIPLMA-2024-YB-10).

References

[1] Avetisyan Daniela,Velizarova Emiliya & Filchev Lachezar. (2022). Post-Fire Forest Vegetation State Monitoring through Satellite Remote Sensing and In Situ Data. Remote Sensing,14(24),6266-6266.

[2] Aakriti Grover & RB Singh. (2016). Monitoring Spatial Patterns of Land Surface Temperature and Urban Heat Island for Sustainable Megacity. Environment and Urbanization Asia,7(1),38-54.

[3] Qian Jing,Armando Marino,Yongjie Ji,Han Zhao,Guoran Huang & Lu Wang. (2024). Spatial and Temporal Change Analysis of Urban Built-Up Area via Nighttime Lighting Data—A Case Study with Yunnan and Guizhou Provinces. Land,13(10),1677-1677.